The 21 May 2021 M_w 6.1 Yangbi Earthquake—A Unilateral Rupture Event with Conjugately Distributed Aftershocks

JunLei Chen[1,2,3], JinLai Hao[*4], Zun Wang[4], and Tao Xu[1,5]

Abstract

An M_w 6.1 earthquake occurred in Yangbi, Yunnan province, China, at 13:48:34 (UTC time) on 21 May 2021. It exhibited a typical foreshock–mainshock–aftershock sequence in the northwestern Yunnan rifting area. We used the first *P*-arrival time from regional broadband seismic stations to check the location of the mainshock's hypocenter. The updated location of the epicenter is 99.88° E, 25.66° N. The focal mechanisms of nine earthquakes, including the mainshock and the largest foreshock and aftershock, were investigated using the general cut-and-paste method based on regional seismic waveforms to set up the fault geometry and to calculate the static coulomb stress change. The rupture process of the mainshock was constrained by 33 unclipped regional broadband seismic records from 15 stations and nine static displacements from three Global Navigation Satellite System stations. The results showed that the Yangbi earthquake was a unilateral rupture event propagating toward the southeast along-strike direction. The moment was 1.81×10^{18} N·m, and the corresponding magnitude was M_w 6.1. The peak slip value, the weighted rupture velocity, and the duration time of the mainshock were 0.95 m, 2.2 km/s, and 9.1 s, respectively. At 10 km southeast of the mainshock's epicenter, the conjugately distributed aftershocks were observed, and the moment density of the mainshock along the strike direction decreased sharply (78% of the total moment released in the first 10 km), suggesting that the sharply decelerating rupture could be the reason for the conjugately distributed aftershocks. The changes in static coulomb stress due to the largest foreshock and mainshock were calculated. The results showed positive Coulomb stress on the major slip zone in the mainshock fault plane triggered by the largest foreshock. Moreover, the 0.01 MPa contour due to the mainshock radiated out of the bend zone of the Weixi–Qiaohou–Weishan fault.

Cite this article as Chen, J. L., J. L. Hao, Z. Wang, and T. Xu (2022). The 21 May 2021 M_w 6.1 Yangbi Earthquake—A Unilateral Rupture Event with Conjugately Distributed Aftershocks, *Seismol. Res. Lett.* **93**, 1382–1399, doi: 10.1785/0220210241.

Introduction

According to the report of the China Earthquake Networks Center (CENC), an M_s 6.4 earthquake (named Yangbi earthquake) struck in Yangbi County, Dali Prefecture, Yunnan Province, China, at 13:48:34 on 21 May 2021 (UTC time). The hypocenter of this earthquake was located at 99.87° E and 25.67° N with a depth of 8 km (CENC). A series of small earthquakes with a maximum magnitude of 4.4 occurred near the epicenter on 18 and 19 May. The largest foreshock with a magnitude of M_s 5.6 occurred at 99.92° E and 25.63° N at 13:21:25 on 21 May, about 27 min before the mainshock. The Yangbi earthquake sequence was a typical foreshock–mainshock–aftershock earthquake sequence, including the largest aftershock with a magnitude of M_s 5.2. According to the research on the regionalization characteristics of historical earthquake types in Yunnan (Huangfu *et al.*, 2007), the percentage of the mainshock–aftershock, the double-mainshocks, and the foreshock–mainshock–-aftershock sequences were 63.2%, 31%, and 5.8%, respectively. And the foreshock–mainshock–aftershock earthquake type had been observed in the northwest Yunnan rifting area.

Northwest Yunnan rift region (Fig. 1) is located at the middle Hengduan Mountain belonging to the southeast margin of the Tethys-Himalayan tectonic domain (Wang *et al.*, 2019). This region is the Yangtze paraplatform and northwest Yunnan geosynclinal fold belt junction area, which has had

1. State Key Laboratory of Lithospheric Evolution, Institute of Geology and Geophysics, Chinese Academy of Sciences, Beijing, China; 2. University of Chinese Academy of Sciences, Beijing, China; 3. Yunnan Earthquake Agency, China Earthquake Administration, Kunming, China; 4. State Key Laboratory of Earth and Planetary Physics, Institute of Geology and Geophysics, Chinese Academy of Sciences, Beijing, China; 5. Innovation Academy for Earth Science, Chinese Academy of Sciences, Beijing, China

*Corresponding author: haojl@mail.iggcas.ac.cn

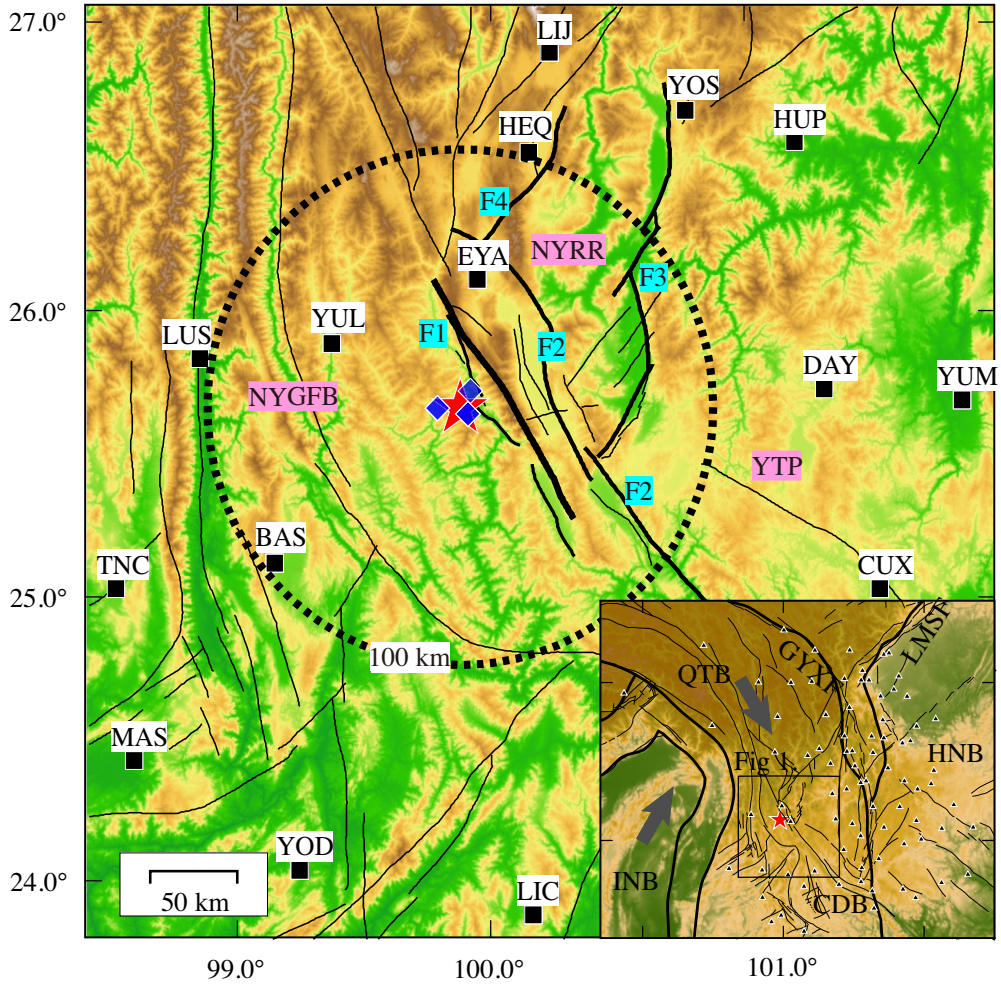

Figure 1. The tectonic background of the Yangbi earthquake sequence. The black squares are broadband seismic stations used in the inversion. The black lines denote the faults in the research area, F1, the Weixi–Qiaohou–Weishan fault; F2, the Red River Fault System; F3, Yongsheng–Binchuan Fault System; F4, Heqin–-Eryuan fault. The abbreviations denote the tectonic units. NYRR, Northwest Yunnan rift region; NYGFB, Northwest Yunnan geosynclinal fold belt; YTP, Yangtze Paraplatform. Three blue diamonds are the used Global Navigation Satellite System (GNSS) stations. The circle denotes the epicentral distance of 100 km. The inset denotes the location of the research area. The triangles in the inset denote the broadband seismic stations used to check the location of the mainshock. The red star denotes the mainshock in both the main figure and the inset. The color version of this figure is available only in the electronic edition.

strong characteristics of structural tension since the Quaternary period (Huang *et al.*, 2014). Therefore, it is called northwest Yunnan rifting basin area, and it developed many different scales rifting basins along the Red River fault system, Heqing-Eryuan fault, and Yongshen-Binchuan fault system (Huang *et al.*, 2014). Large earthquakes frequently occurred in the northwest Yunnan rifting region (Li *et al.*, 2016). Since 1498, nine destructive earthquakes of M 6.0+ were reported, including two earthquakes of M 7.0+. According to the research on the characteristics of geothermal and tectonic activity in the northwest Yunnan rifting area (Wang *et al.*, 2019), the geothermal and earthquake activity in the northwest Yunnan rifting area were not only the result of fault activity but also related to the regional dynamic process and deep hot magma and fluid activity. The Yangbi earthquake sequence is a good example for investigating the source physical process and the source area rupture characteristics in the northwest Yunnan rift region.

From 21 to 29 May 2021, CENC report that this earthquake cluster had 46 earthquakes of M 3.0+, including one earthquake of magnitude 6.0–6.9, three earthquakes of magnitude 5.0–5.9, 13 earthquakes of magnitude 4.0–4.9. The number and magnitude of aftershocks decay slowly with time (Liu *et al.*, 2021; Su *et al.*, 2021; Wang, Hu, *et al.*, 2021). Some researchers had reported the slip model of the mainshock based on geodetic data, including Global Navigation Satellite System (GNSS) and Interferometric Synthetic Aperture Radar (InSAR) data. The Institute of Geophysics, China Earthquake Administration (CEA) released the Yangbi earthquake emergency support of science and technology briefing on 22 May (Zhang *et al.*, see Data and Resources). Teleseismic data were applied to constrain the rupture process. However, the magnitude of this earthquake was too small to have an excellent rupture model by the teleseismic data. Regional broadband seismic stations and GNSS stations recorded this earthquake very well (Fig. 1). In this study, we checked the location of the mainshock's hypocenter by regional first P-arrival times. The general cut-and-paste (gCAP; Zhu and Ben-Zion, 2013) method was used to obtain the focal mechanisms of the mainshock, large foreshocks, and large aftershocks, respectively. The rupture process of the mainshock was constrained by regional broadband waveforms and

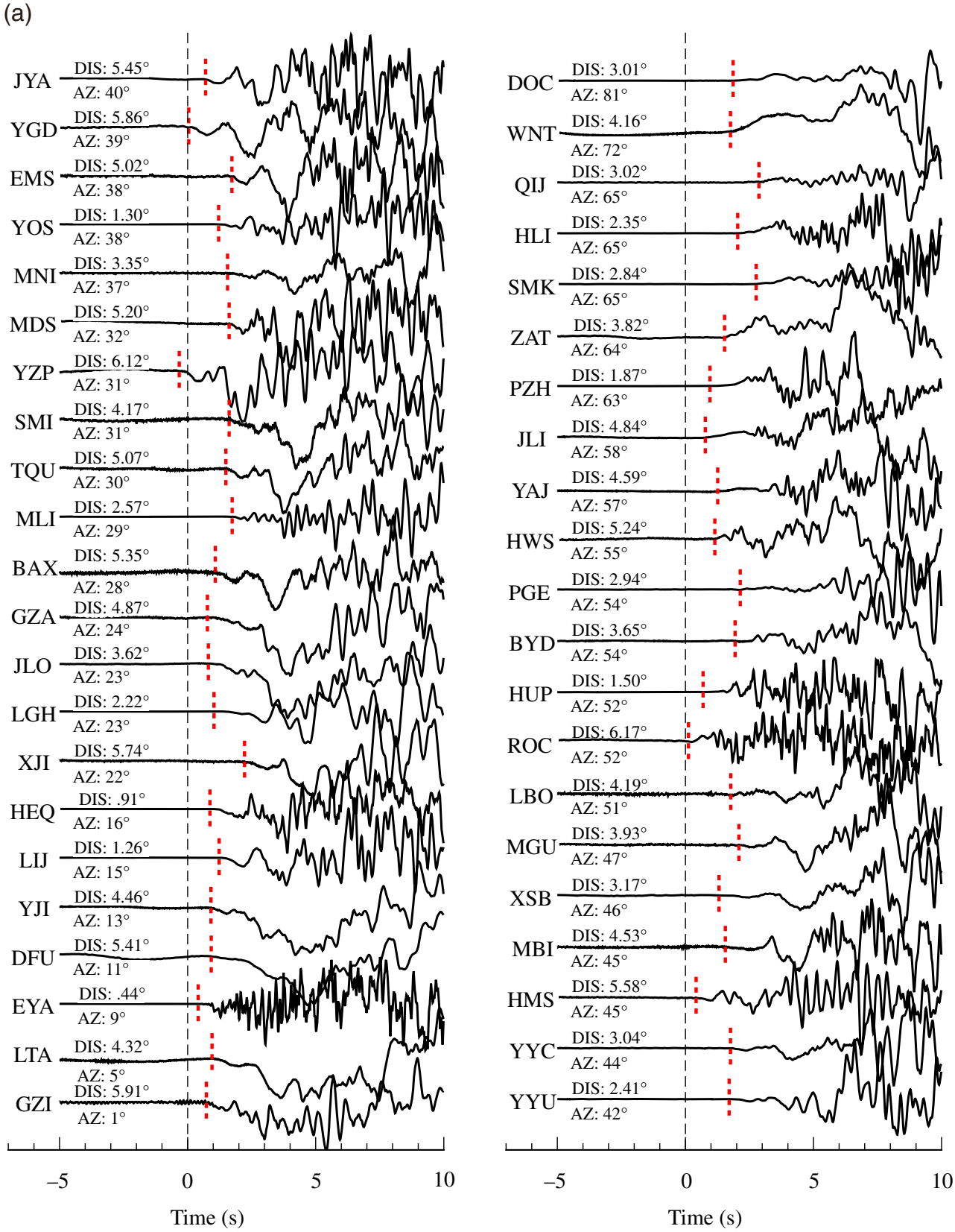

Figure 2. The picked *P*-arrival time (red dot) profile of the mainshock. (a) The result of the first 41 records. The black dashed lines denote the synthetic *P*-arrival time. The names of stations are plotted at the left. The epicentral distance (°) and azimuth (°) are plotted above and below the waveforms, respectively. (b) The result of the other records. The color version of this figure is available only in the electronic edition. (*Continued*)

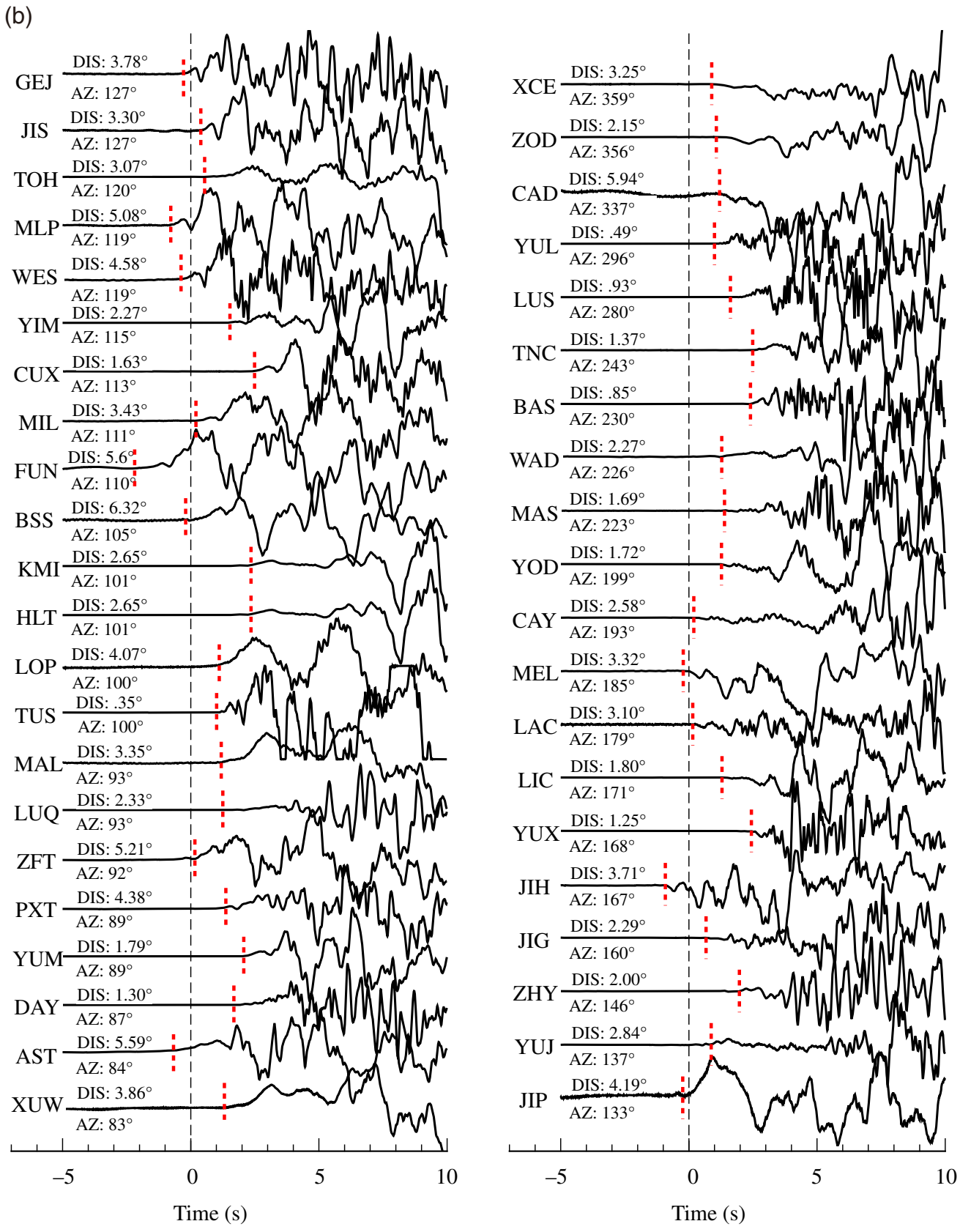

Figure 2. Continued

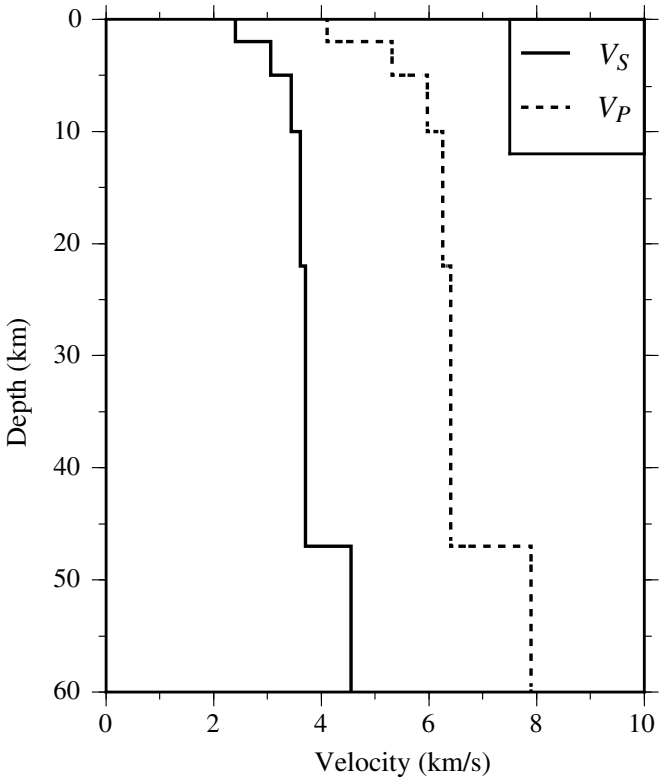

Figure 3. The crustal velocity model used to calculate Green's function. The solid and dotted lines denote *S*- and *P*-wave velocity, respectively.

GNSS data. Then, the static coulomb stress change of the foreshock and the mainshock was calculated to analyze the stress interaction and the triggering in the Yangbi earthquake sequence.

Hypocenter and Focal Mechanism

We used the first *P*-arrival time of regional broadband seismic stations with epicentral distances of less than 6.5° (Fig. 1) to check the location of the mainshock's hypocenter to begin this study. We picked up the first *P*-arrival time of raw waveforms in the vertical component (Fig. 2). Based on the Crust 2.0 (Bassin *et al.*, 2000) and the results of active source seismic imaging (Xu *et al.*, 2014; Xu, Zhang, Liu, *et al.*, 2015), the 1D crustal velocity model was established and adopted in this article (Fig. 3). We calculated the synthetic first *P*-arrival time by tauP (Crotwell *et al.*, 1999) and set up a regional synthetic *P*-arrival time table. The epicentral distance and depth intervals were 0.1° and 0.5 km, respectively. A grid-search method was applied to determine the hypocenter with the least residual misfit (Ye *et al.*, 2017). The search domain and intervals are shown in Table 1. Figure 4 shows the result of the relocated hypocenter of the mainshock. The new epicenter (cyan star in Fig. 4a) was about 1.5 km southeast of the epicenter of the CENC (red star in Fig. 4a). The longitude, latitude, and depth of the new hypocenter were 99.88°, 25.66°, and 11.5 km, respectively. Although the misfit had the least value at a depth of 11.5 km (Fig. 4b), the depth resolution in the shallow crust was not well constrained. The residual time of the hypocenter of CENC was a 1.27 s variance, and it decreased to a 0.78 s variance of the new hypocenter. There was no significant trend of the residual time with the epicentral distance and azimuth (Fig. 4c,d).

TABLE 1
Grid-Search Domain and Interval of the Mainshock's Hypocenter

Parameters	Search Domain	Interval
Latitude (°)	25.52–25.82	0.01
Longitude (°)	99.72–100.02	0.01
Depth (km)	5.0–20.0	0.5
Origin time (s)	−3.0 to 3.0	0.1

We applied the gCAP method to the regional broadband seismic data to obtain the focal mechanism solutions of nine events in the Yangbi earthquake sequence (Table 2). Figures 5–7 show the waveform comparison of the main earthquake, the M_s 5.6 largest foreshock, and the M_s 5.2 largest aftershock, respectively. The frequency–wavenumber method (Zhu and Rivera, 2002) was utilized to calculate Green's function, and the velocity model is shown in Figure 3. The regional broadband seismic waveforms would be clipped. Therefore, we checked the seismic records of regional broadband stations and selected 14 regional broadband stations with high signal-to-noise ratios and unclipped amplitude with epicenteral distance between 55.4 and 287.4 km to constrain the focal mechanism solution of the mainshock. For the largest foreshock and aftershock, the number of available stations was increased to 21 with epicenteral distance between 53.1 and 289.5 km for M_s 5.6 and 24 with epicenteral distance between 57.5 and 240.3 km for M_s 5.2, respectively. The raw data were deaveraged and detrended, and the instrument response was removed to velocity waveforms. Then the *E* and *N* components of raw data were rotated to the *R* and *T* components. In the inversion, the synthetic waveforms and the observed data of three components were calculated and resampled with a 0.1 s interval, respectively. Meanwhile, the synthetic and observed waveforms were bandpass filtered by 0.05–0.2 Hz for the *Pnl* wave and 0.02–0.1 Hz for the surface wave. The search domain of centroid depth varied from 2 to 20 km with an interval of 2 km. The search domain of strike (θ), dip (δ), and rake (λ) varied from 0° to 360°, 0° to 90°, and −180° to 180° with an interval of 5°, respectively.

The focal mechanism results show that the moment of the mainshock is 1.2×10^{18} N · m, and the moment magnitude of the mainshock is M_w 6.0 based on the equation of Kanamori (1977). The correlation coefficients between synthetic and

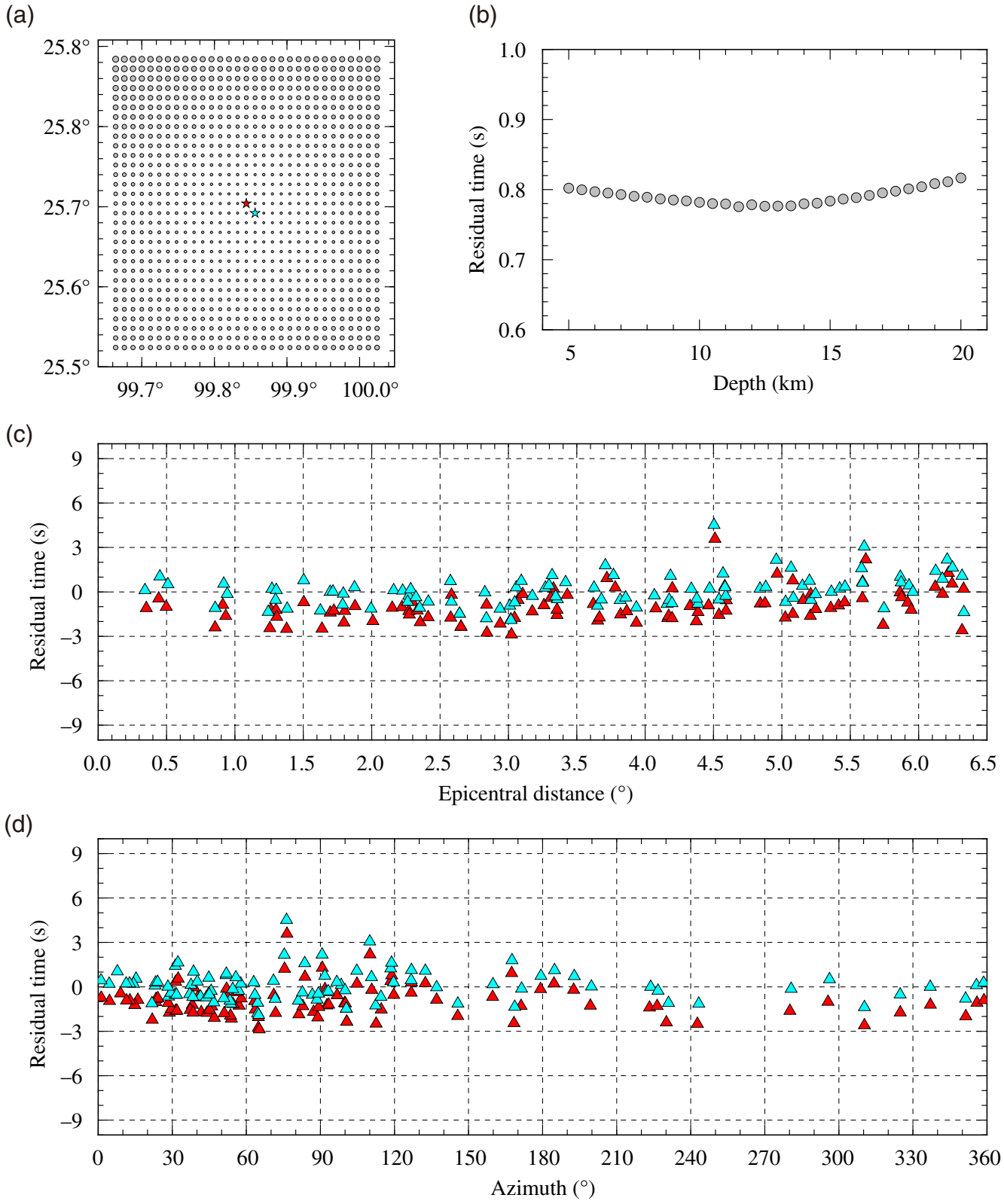

Figure 4. Relocation of the hypocenter for the mainshock using handpicked *P* arrivals in the vertical component of stations within 6.5°. (a) Map view of misfit of *P* arrivals for variable assumed epicenters (gray dots). The red and cyan stars are the China Earthquake Networks Center's (CENC) epicenter and this study's epicenter, respectively. (b) Misfits versus different hypocenter depths. (c) Residual time along with epicentral distance profile. Red triangles and cyan triangles represent the result of CENC's epicenter and this study's epicenter at each station, respectively. (d) Residual time along with azimuth profile. Red triangles and cyan triangles represent the result of CENC's epicenter and this study's epicenter at each station, respectively. The color version of this figure is available only in the electronic edition.

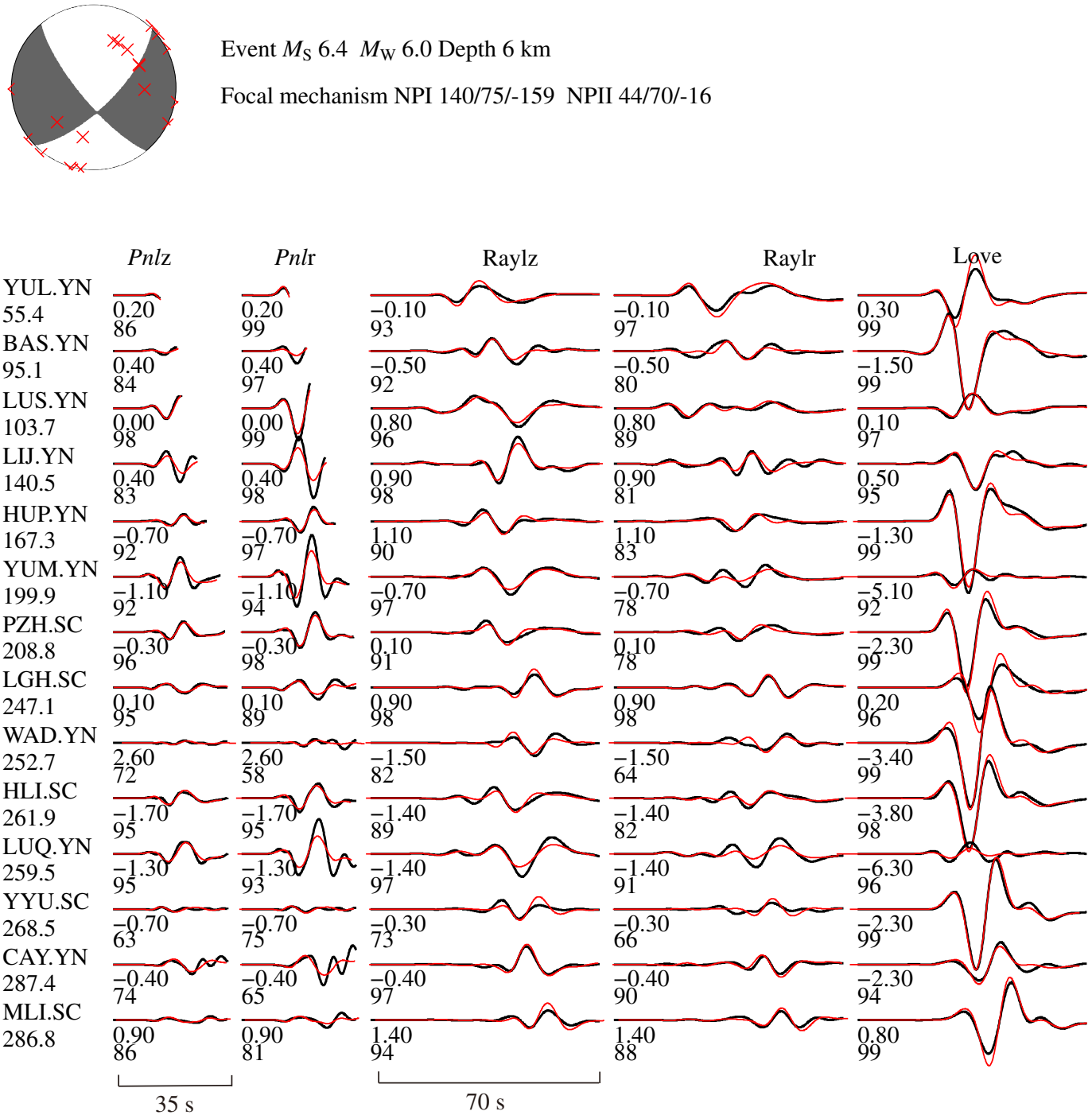

Figure 5. The focal mechanism and waveforms fitting of the mainshock. The station name and epicentral distance (km) are marked on the left of observed records (black), and synthetic waveforms (red). The values under the waveforms denote the time shift and cross-correlation coefficient. The color version of this figure is available only in the electronic edition.

observed waveforms at 90% of stations were over 80% (Fig. 5). Most of the time shifts of the *Pnl* and surface wave were less than 2.0 s, indicating that the crustal velocity model was appropriate. Two node planes (NP I and NP II) of the focal mechanism solution of the mainshock were 140°/75°/−159° and 44°/70°/−16°, respectively, which was consistent with the result by the full waveform fitting method (138°/81°/−160° and 45°/70°/−10°; Yang *et al.*, 2021). The focal mechanism solutions (NP I and NP II) of the largest foreshock and aftershock (Figs. 6 and 7) were 317°/58°/−150° and 210°/65°/−36°, respectively, and 148°/46°/−155°, and 40°/72°/−47°, respectively. There were noticeable normal components of the focal mechanism solutions. The misfit of the mainshock had a minimum value at the centroid depth of 6 km (Fig. 8). The moment

TABLE 2
Focal Mechanism Solutions of Nine Events in the Yangbi Earthquake Sequence

		Epicenters*		Focal Mechanisms			
Number	Time (yyyy/mm/dd hh:mm:ss)	Longitude (°)	Latitude (°)	NP I Strike/Dip/ Rake (°)	NP II Strike/Dip/ Rake (°)	M_w	Depth (km)
1	2021/05/18 21:39:37	99.92	25.64	307/79/161	41/71/12	4.2	6
2	2021/05/19 20:05:56	99.91	25.65	318/71/180	48/90/19	4.6	6
3	2021/05/21 20:56:03	99.91	25.61	152/47/–128	21/55/–57	4.2	5
4	2021/05/21 21:21:26	99.92	25.65	317/58/–150	210/65/–36	5.3	6
5	2021/05/21 21:48:35	99.88	25.70	140/76/–159	45/70/–15	6.0	6
6	2021/05/21 22:31:12	99.97	25.61	148/46/–155	40/72/–47	5.0	8
7	2021/05/22 09:48:01	99.89	25.70	314/79/–165	221/75/–11	4.1	4
8	2021/05/22 20:14:36	99.92	25.60	322/43/–144	204/66/–53	4.6	6
9	2021/05/27 19:52:48	99.92	25.76	288/66/–163	191/75/–25	4.1	4

*From China Earthquake Networks Center (CENC).

magnitude of the largest foreshock and aftershock were M_w 5.3 and 5.0, and the corresponding moments were about 1.1×10^{17} N · m and 3.9×10^{16} N · m, respectively. They had similar centroid depths as the mainshock (6 km for foreshock and 8 km for aftershock in Fig. 8).

Finite-Fault Inversion

We used the same regional stations (33 unclipped components of 15 regional broadband stations) and three GNSS stations to constrain the rupture process of the mainshock (Fig. 1). Zhang *et al.* (2021) obtained the static displacements of 35 GNSS stations covering the Yangbi earthquake. Three stations had displacements larger than 3 cm, which were used in this study. Nevertheless, the displacement waveforms and a higher corner frequency were applied. After removing the instrument response of the observed data, a Butterworth band-pass filter was applied to filter the displacement waveforms with a 0.02–0.5 Hz frequency range. We resampled all observed records to 0.1 s with the same interval to synthetic data. The frequency–wavenumber method (Zhu and Rivera, 2002) was applied to calculate Green's function based on our crustal velocity structure (Fig. 2). The Generalized reflection–transmission coefficient matrix method was used to calculate Green's function of static displacement (Xie and Yao, 1989; Hao and Yao, 2012).

In this article, a finite-fault inversion method based on simulated annealing (Ji *et al.*, 2002a,b, Hao *et al.*, 2013, 2017) was adopted. By matching the waveform in the wavelet domain, the source parameters such as slip, rake angle, rise time, and rupture velocity of the earthquake could be determined effectively using the nonlinear inversion method. Based on the relocated hypocenter and focal mechanism result of the mainshock, the node plane, striking 140° and dipping 75°, was selected as the causal fault plane. The fault plane was 28 km along the strike direction and 18 km along the dip direction, and the subfault size was 2 km × 2 km. The hypocenter was located at the subfault (number 3 along-strike direction and number 4 along the dip direction). The depth of the hypocenter was set to 11 km, which referred to the focal depth of relocation. The search domain of slip, rake angle, rupture velocity, and rise time were 0–1.2 m, 135°–195°, 1.25–3.75 km/s, 0.2–1.4 s, respectively. After a series of preliminary tests, the weighting factor between GNSS data and the seismic data was chosen as 0.2.

After calculating Green's function, data preprocessing, and finite-fault model parameterization, we inverted for the source rupture process of the mainshock (Fig. 9). The source rupture process result showed that the weighted rake angle was 189°, which means that this earthquake was a nearly pure strike-slip earthquake. The scalar seismic moment was 1.81×10^{18} N · m, and the moment magnitude was M_w 6.1, according to the equation of Kanamori (1977). The centroid depth was 7.6 km, which was consistent with the point-source focal mechanism solution by gCAP. Moreover, it showed that the Yangbi earthquake was a unilateral rupture event. The dominant slip patch (slip patch with more than 25% of the peak slip) was centered in the southeast of the epicenter, whereas the rupture was not apparent in the northwest of the epicenter. The relocation of aftershocks (Su *et al.*, 2021) shows that the large aftershocks mainly expanded to the southeast of the epicenter, which is consistent with the rupture directivity. The peak slip value of the main earthquake was 0.95 m. The rupture was relatively concentrated, and the dominant slip patch was about 18 km along the strike direction and 8 km along the dip direction. A total of 95% of moment released in the first 9.1 s.

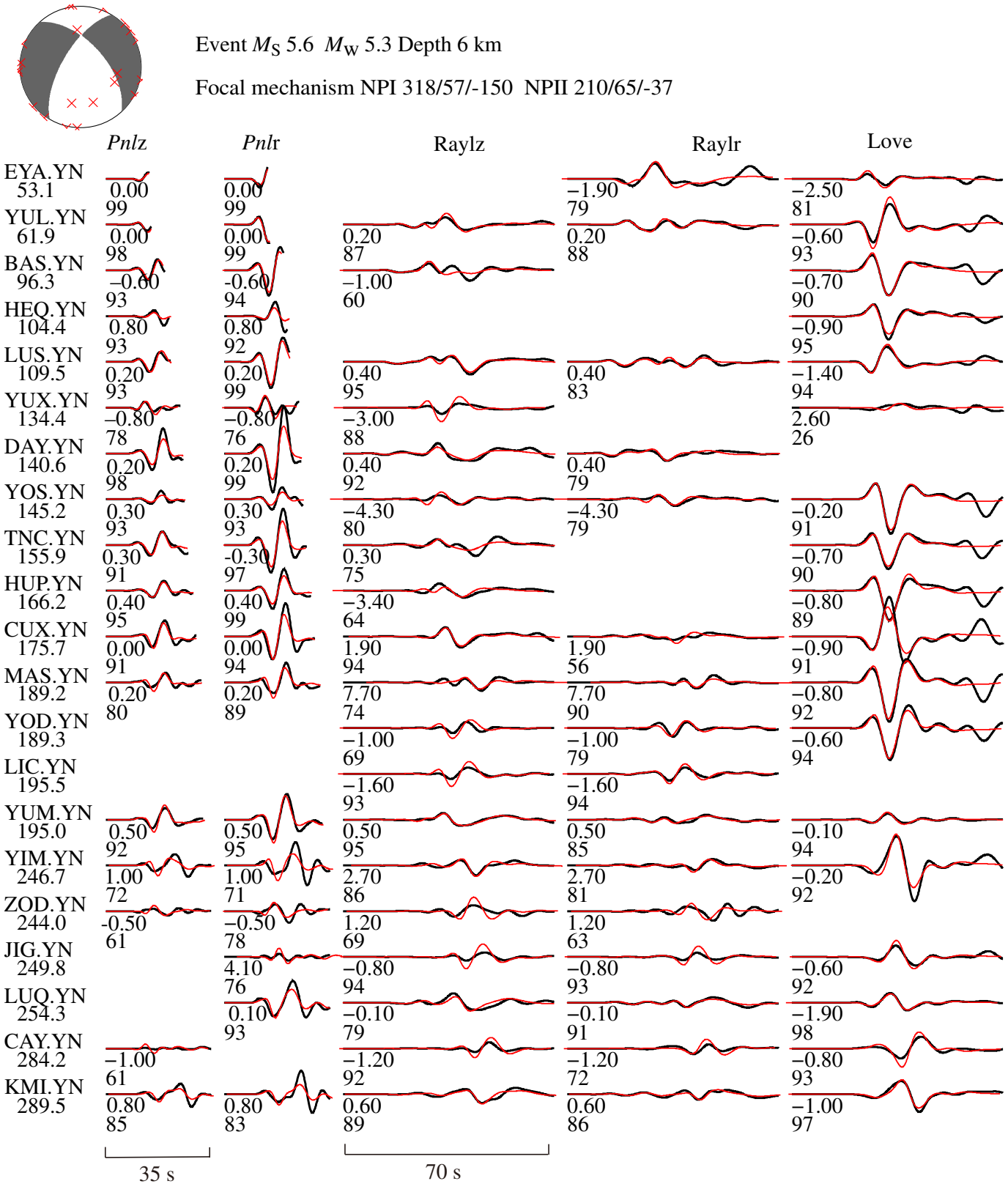

Figure 6. The focal mechanism and waveforms fitting of the M_s 5.6 foreshock. Other notes are the same as Figure 5. The color version of this figure is available only in the electronic edition.

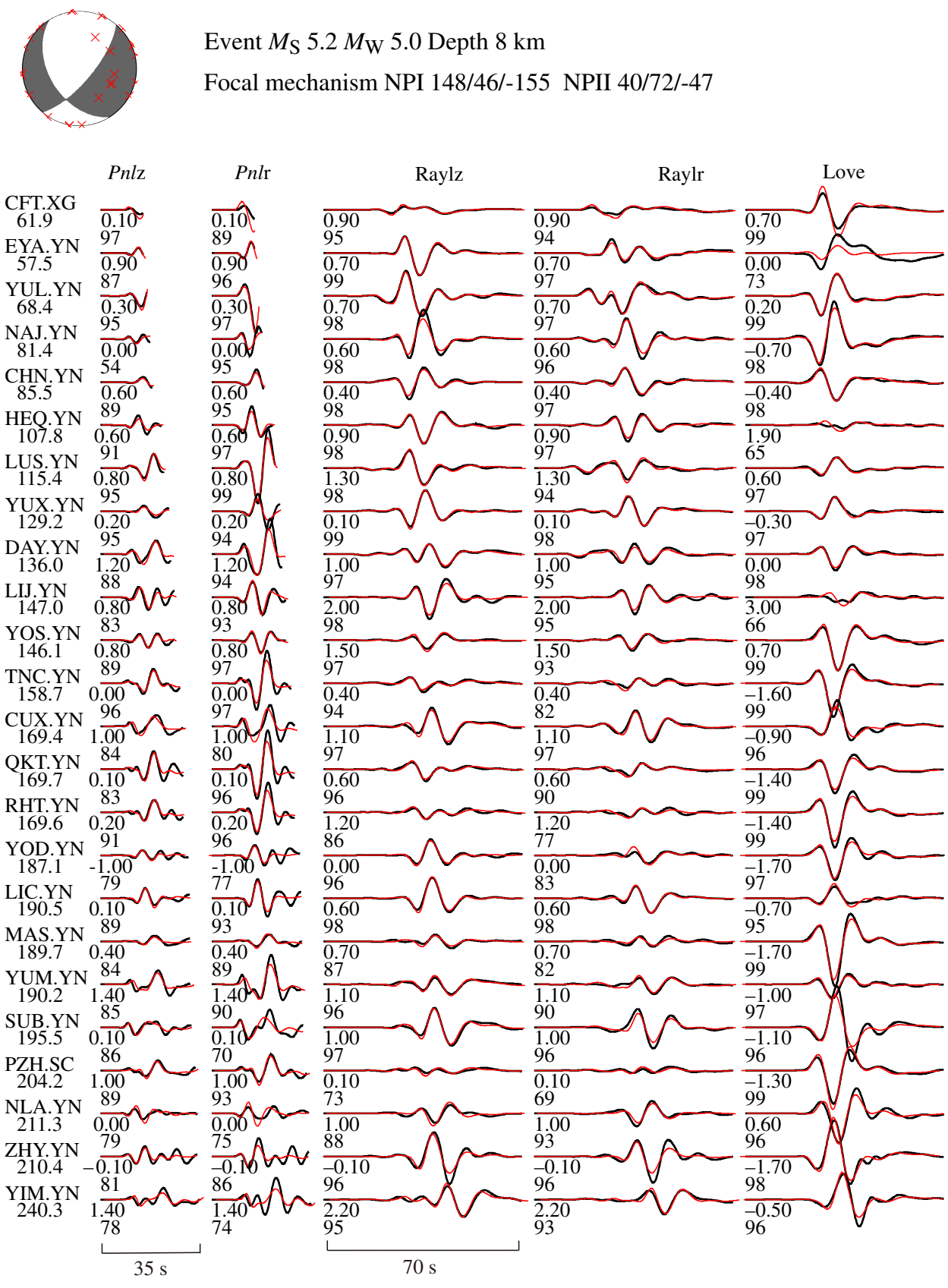

Figure 7. The focal mechanism and waveforms fitting of the M_s 5.2 aftershock. Other notes are the same as Figure 5. The color version of this figure is available only in the electronic edition.

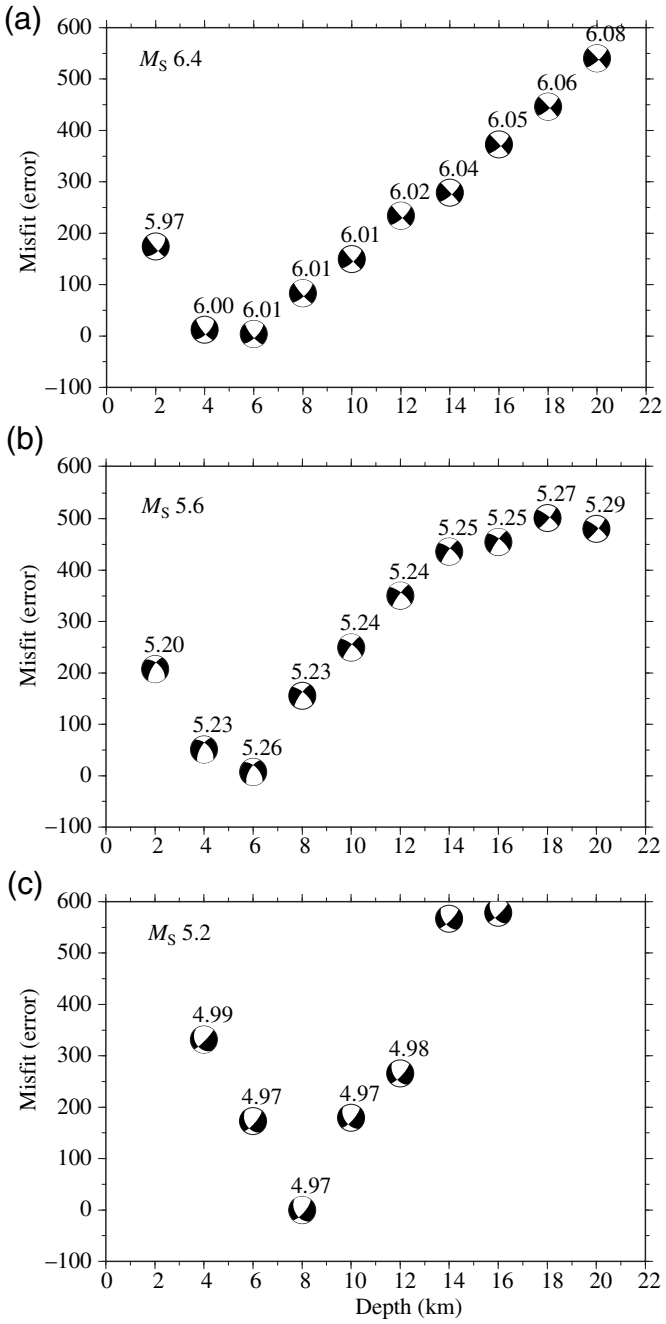

Figure 8. The focal mechanism solutions and misfits with different fitting depths. (a–c) The mainshock, M_s 5.6 foreshock, and M_s 5.2 aftershock, respectively. The value on the top of the focal mechanism is the moment magnitude.

The weighted rupture velocity was approximately 2.2 km/s, and the weighted rise time was approximately 0.8 s. We used our slip model to calculate the stress drop of the Yangbi earthquake (Fig. 9) by an analytical expression of stress in the homogeneous half-space (Okada, 1992). The energy-based average stress drop (Shao *et al.*, 2012; Adams *et al.*, 2019) along-strike 140° was approximately 2.2 MPa.

Static Stress Interaction

The Yangbi earthquake had a series of foreshocks and complex aftershock distribution. To evaluate the interaction of the foreshock, mainshock, and aftershock, we calculated the static coulomb stress change of the largest foreshock and the mainshock (Okada, 1992). The relative positions of the largest foreshock and mainshock by Su *et al.* (2021) were adopted. We calculated the static coulomb stress change in the mainshock's causal fault plane due to the largest foreshock. In the calculation, the velocity of *P*-wave, density, Poisson's ratio, and Young's modulus were 6.2 km/s, 2.85 g/cm^3, 0.25, and 9.1 GPa, respectively. According to the relationship between the fault-slip accumulation and the effective friction coefficient (Parsons *et al.*, 1999), the effective friction coefficient was set to 0.4 in this research (Lin and Stein, 2004). Assuming that the largest foreshock occurred on a uniform fault of 3 km × 3 km, the slip was calculated to be 0.12 m by the moment. The inverted focal mechanism of the largest foreshock was applied. The change of static coulomb stress based on the two nodal planes is shown in the left and right panels of Figure 10, respectively.

Because of the uncertainty of the location of the epicenter and the rupture directivity, we moved the mainshock fault plane to the south by 1 km and 2 km, respectively, resulting in three fault planes: F1, F2, and F3. The third fault plane (F3) was used in our finite-fault inversion. The static coulomb stress change in the three faults was calculated. Generally, the two nodal planes of the largest foreshock resulted in two different patterns in the mainshock's fault plane. If the foreshock occurred on NP II (strike 318°, right column in Fig. 10), then the static coulomb stress in most of the mainshock's fault plane would increase. In contrast, the static coulomb stress on the shallow fault would decrease due to the other node plane (strike 210°, left column in Fig. 10). Generally, the largest foreshock increased the static coulomb stress in the rupture zone with a large slip value near the epicenter. The results suggest that the largest foreshock promoted the occurrence of the mainshock.

Based on our joint finite-fault slip model, we calculated the static coulomb stress change at different depths. The same elastic modulus and the effective friction coefficient were adopted. We divide the study region into two parts. The dip and rake angles of mainshock's focal mechanism are applied at the northern part. But we change the strike angle from 170° to 140° southward gradually to evaluate the effect of mainshock on the known fault—the Weixi–Qiaohou–Weishan fault. Two nodal planes of the top two largest aftershocks are applied to evaluate the aftershock triggering of the possible conjugately distributed faults (Fig. 11a,b). Figure 11c–h shows the results at depths of 4 km, 7 km, and 10 km, respectively. The contour with 0.01 MPa is highlighted in the figure. Generally, the 0.01 MPa contour radiated out of the bend zone of the Weixi–Qiaohou–Weishan fault. Therefore, the effect of the

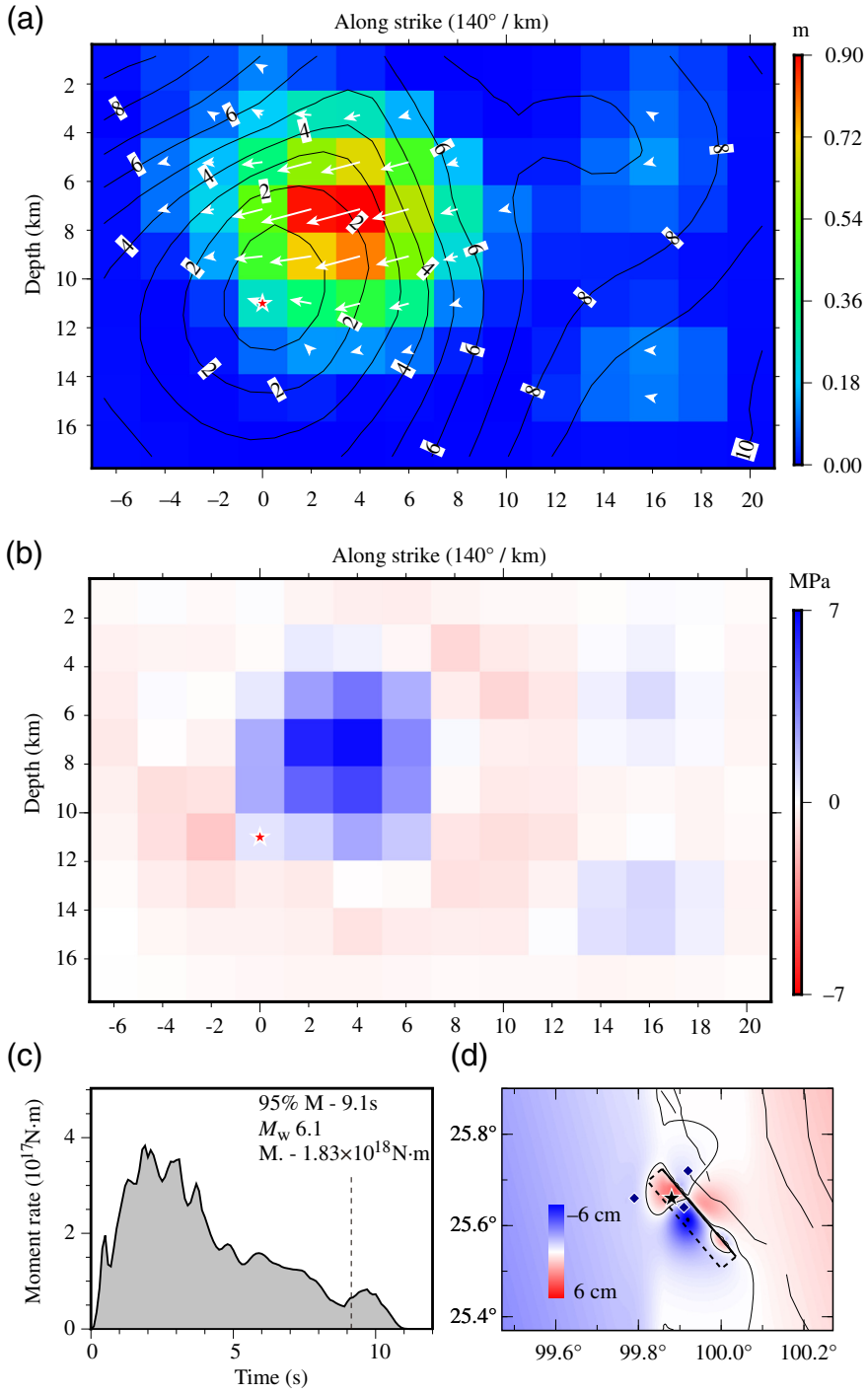

Figure 9. Joint inversion model of the Yangbi earthquake. (a) The slip distribution of the Yangbi earthquake. The black contour and number denote the location rupture front and the initial rupture time. The white arrows denote the slip direction, and the color shows the slip value. (b) The stress drop of the mainshock according to the slip distribution of (a). (c) The moment rate of the mainshock. (d) The synthetic vertical displacement with the three used GNSS stations. (e,f) The vertical and horizontal Global Positioning System displacement, respectively. The black and red arrows represent the observed and synthetic static displacement, respectively. (g) The waveforms fitting of the finite-fault inversion. The station name and azimuth (°) are marked on the top left of observed records (black) and synthetic waveforms (red). At the left bottom of waveforms, the component and epicentral distance (km) are denoted. The numbers on the top right of waveforms denote the peak amplitude value of waveforms with the unit in centimeters. The color version of this figure is available only in the electronic edition. (*Continued*)

Yangbi earthquake on known faults was limited. The change of static coulomb stress due to the mainshock consists of the distribution of aftershocks distribution generally. Regardless of the nodal plane that is chosen to project the calculated Coulomb stress change, the Coulomb stress change shows a similar pattern (Fig. 11c–h). The static coulomb stress increased at the southeast end of the slip zone of the mainshock, where large aftershocks occurred correspondingly.

Discussion and Conclusions

Our joint inversion model slip distribution generally consisted of finite-fault models constrained by geodetic data. According to the preliminary InSAR inversion (see Data and Resources) of the Institute of Geology, CEA, the results show that the seismogenic fault that produced the Yangbi earthquake has a fault strike of 138°, dips to the southwest, and has a dip angle of 80°, which is consistent with our focal mechanism of NP I with a fault strike of 140° and a dip of 75°. The GNSS inversion (Zhang *et al.*, 2021) showed that coseismic slip was mainly distributed at depths between 3 and 12 km. A joint inversion model constrained by GNSS and InSAR data (Wang, Liu, *et al.*, 2021) achieved a slip model concentrated at a depth of 2–10 km. The moment magnitude of these two models was M_w 6.0, and the peak slip was close to 0.8 m. In this article, the rupture process of the Yangbi earthquake was constrained by regional broadband seismic and GNSS data.

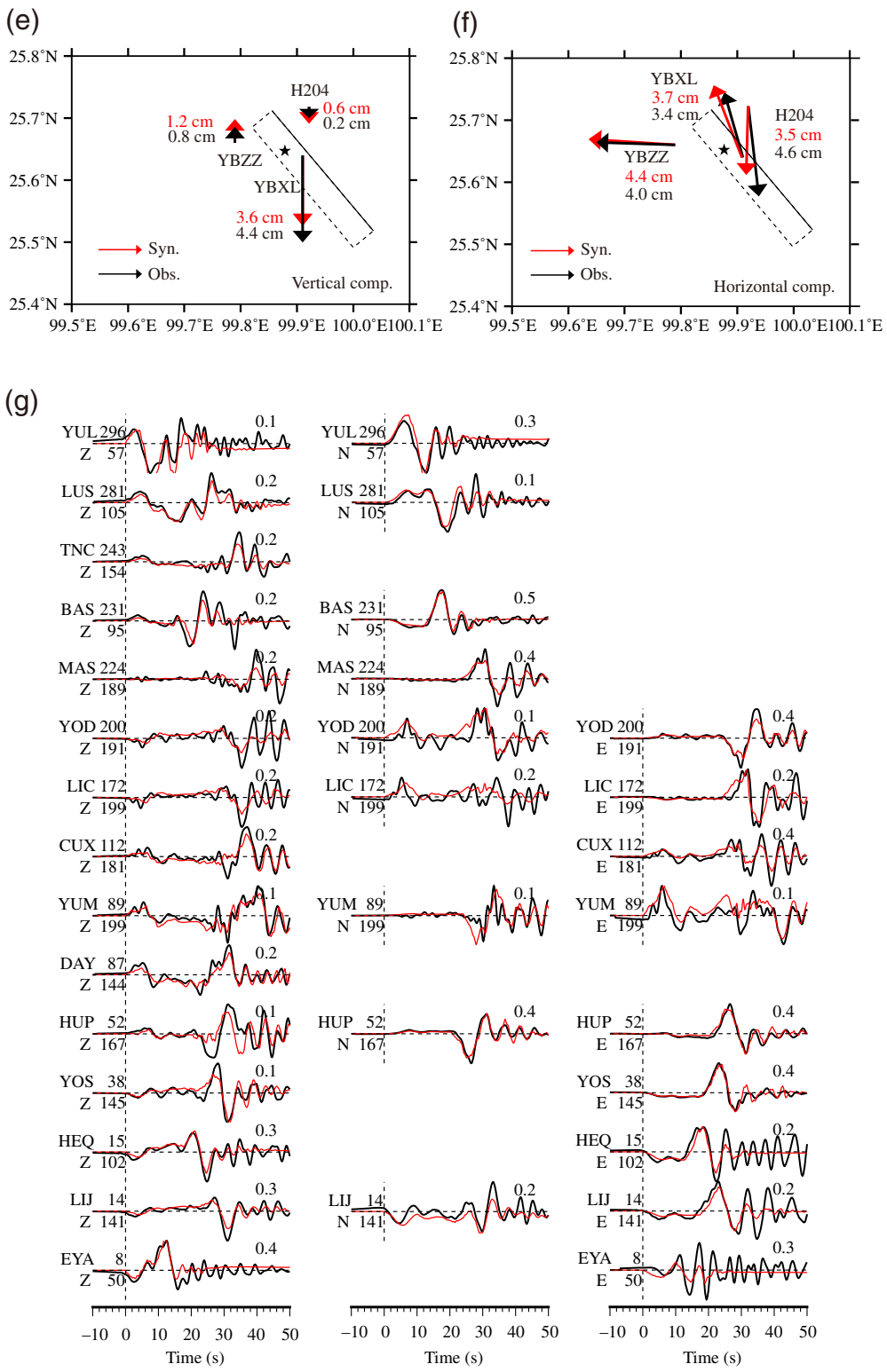

Figure 9. Continued

The results showed a coherent magnitude of M_w 6.1 and peak slip value (0.95 m). The slip expanded from 4 to 12 km, which was slightly deeper than the depth range of the geodetic model. The field investigation (Li *et al.*, 2021) did not observe obvious surface rupture. The relocation of the Yangbi earthquake sequence (Long *et al.*, 2021; Su *et al.*, 2021) showed that the long axis of dominant aftershocks was approximately 22 km, striking northwest–southeast. It was approximately 5–10 km away from the Weixi–Qiaohou–Weishan fault, which is located on the southwestern border of the rifting basin in northwest Yunnan. Therefore, the seismogenic fault of the Yangbi earthquake is a parallel secondary structure of the Weixi–Qiaohou–Weishan fault that did not expand to the surface. The M_w 6.1 Yangbi earthquake was a blind fault event. The ground surface is a possible condition to induce super-shear rupture of a strike-slip event (Xu, Zhang, and Chen, 2015). This indicates that strike-slip earthquakes that rupture to the surface are more likely to cause greater disaster damage.

The epicenter of mainshock in this study is about 3 km from the result of Su *et al.* (2021), which results from the different velocity model, phase picking, and method. We use the mainshock as the reference to discuss the relationship between the mainshock's rupture and the aftershock distribution. Therefore, we move the whole catalog of Su *et al.* (2021) to make the two epicenters of mainshocks coincide entirely. Figure 12 shows the projection

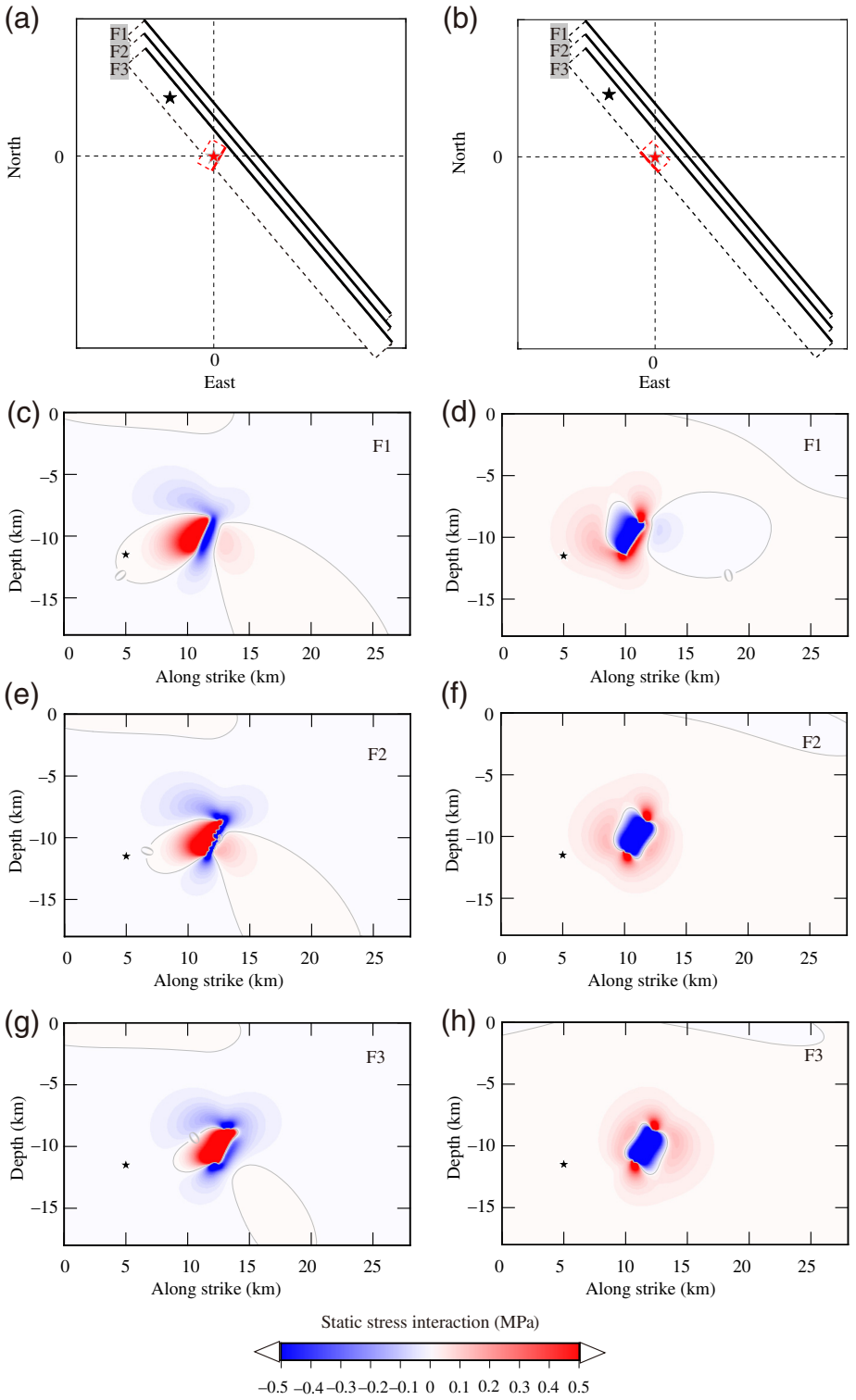

Figure 10. The static coulomb stress change due to the largest M_w 5.3 foreshock. (a) The map view of the mainshock's and foreshock's fault planes. The black rectangle and star denote the mainshock's fault plane and epicenter, respectively. The red rectangle and star represent the foreshock's fault plane and epicenter, respectively. The fault plane F1 (our used finite-fault plane) is moved toward the south by 1 km and 2 km, resulting in F2 and F3, respectively. (c,e,g) Change of the static coulomb stress due to the largest M_w 5.3 foreshock on F1–F3, respectively. (b,d,f,h) Results of the other nodal plane of the largest foreshock. The color version of this figure is available only in the electronic edition.

of aftershocks in the depth profile with a magnitude larger than M 3 within one day after the mainshock (catalog from Su *et al.*, 2021). Large aftershocks occurred around the large slip patch where the static coulomb stress increased. Previous studies have widely reported the relationship between seismic slip areas and aftershock distributions (Yamanaka and Kikuchi, 2004; Ji *et al.*, 2015; Wei *et al.*, 2018). Yamanaka and Kikuchi (2004) investigated the source processes of large earthquakes in northeastern Japan and revealed that aftershocks occurred in the area surrounding the asperity (fig. 9 in Yamanaka and Kikuchi, 2004).

The conventional Mohr–Coulomb faulting theory suggests that faults form conjugate faults with an acute angle along the principal compression axis (Anderson, 1951). For values of the coefficient of friction of 0.6–0.8, the angles between conjugate planes are approximately 50°–60° (Thatcher and Hill, 1991; Fialko and Jin, 2021). However, an increasing number of observations revealed high-angle conjugate faults (Thatcher and Hill, 1991; Yue *et al.*, 2012; Ross *et al.*, 2019; Fialko and Jin, 2021), such as orthogonal faults in the 2019 Ridgecrest earthquake. Two typical models for producing the high-angle conjugate faults have been developed, including rotation of faults in the brittle crust and influence of ductile faulting in the layer beneath (Thatcher and Hill, 1991; Ross *et al.*, 2019; Fialko and Jin, 2021). A dynamic rupture effect near rupture edges could result in cross faults based on

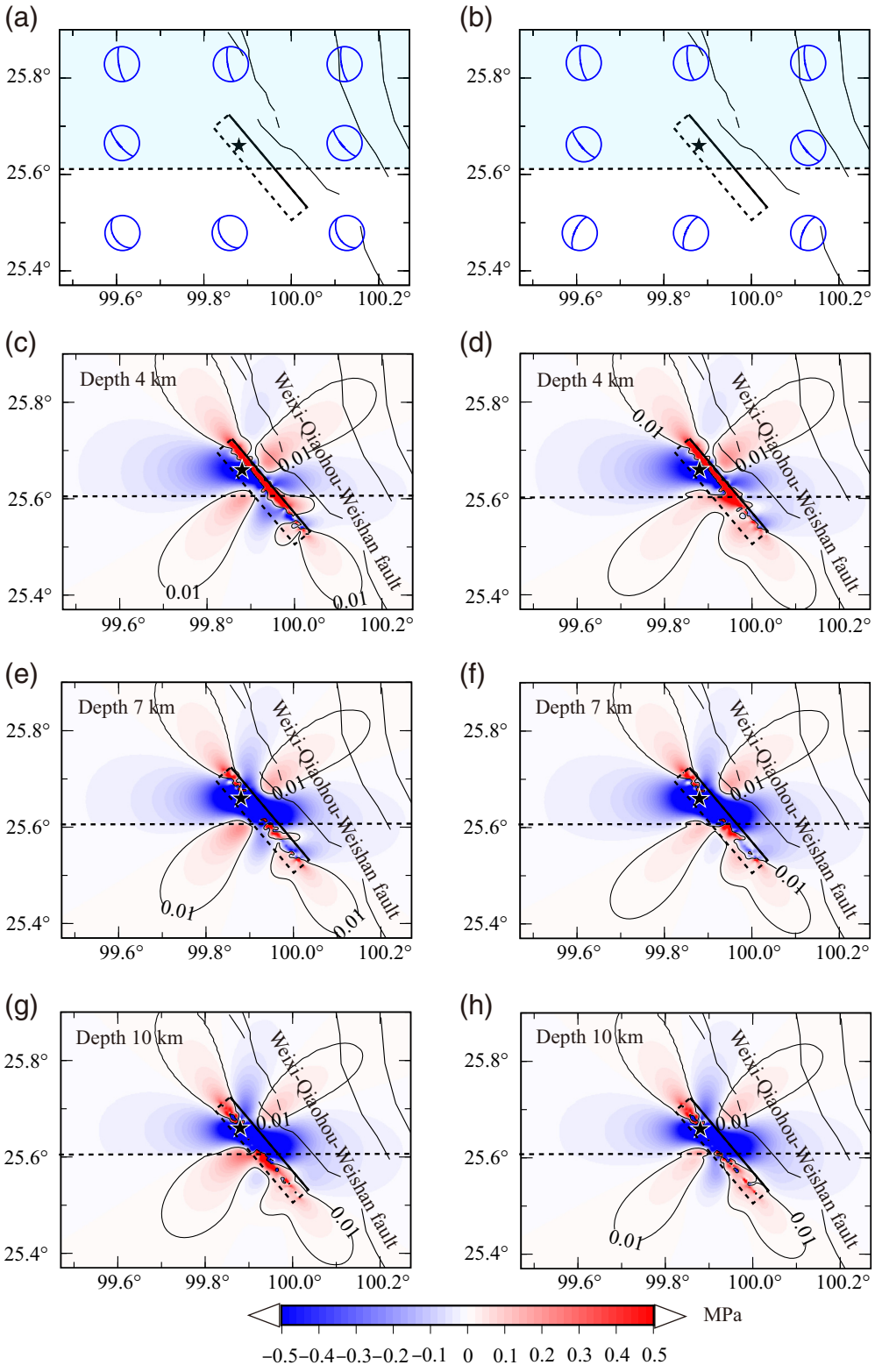

Figure 11. The static coulomb stress change of the mainshock. Two receiver nodal planes are applied. (a,b) The nodal planes used to calculate the static coulomb stress change. (a,c,e,g) Coulomb stress change at depths of 4 km, 7 km, and 10 km, respectively, based on the nodal planes in (a). (b,d,f,h) Coulomb stress change at depths of 4 km, 7 km, and 10 km, respectively, based on the nodal planes in (b). The black rectangle and star denote the causal fault plane and location of the mainshock, respectively. The 0.01 MPa contour is highlighted. The color version of this figure is available only in the electronic edition.

recent numerical simulations (Xu and Ben-Zion, 2013; Xu, 2020; Okubo *et al.*, 2019). Su *et al.* (2021) adopted a deep-learning algorithm, PhaseNet, a rapid earthquake association and location method, and multiple earthquake location methods to obtain a high-resolution catalog of the Yangbi earthquake (Fig. 12, three days before the mainshock and seven days after the mainshock). A series of conjugately distributed aftershocks could be observed at approximately 10–20 km southeast of the mainshock's epicenter. The angle between two conjugating faults decreases along the strike direction (Fig. 12). At 10 km southeast of the mainshock's epicenter, the faults are close to orthogonal planes where the angle is significantly larger than the typical value of 50°–60°. In this study, the moment density of the mainshock along-strike direction decreased sharply at approximately 10 km southeast of the epicenter (78% of total moment released in the first 10 km), implying that the sharply decelerating rupture produced conjugately distributed aftershocks. In contrast, at the southeastern end of the Yangbi earthquake sequence, the angle is close to the typical acute angle predicted by the conventional Mohr–Coulomb faulting theory.

Data and Resources

The regional broadband data were obtained from the Data Management Centre (DMC) of China National Seismic Network at the Institute of Geophysics China Earthquake Administration (CEA). The coseismic displacements of Global Navigation Satellite System (GNSS) stations were obtained

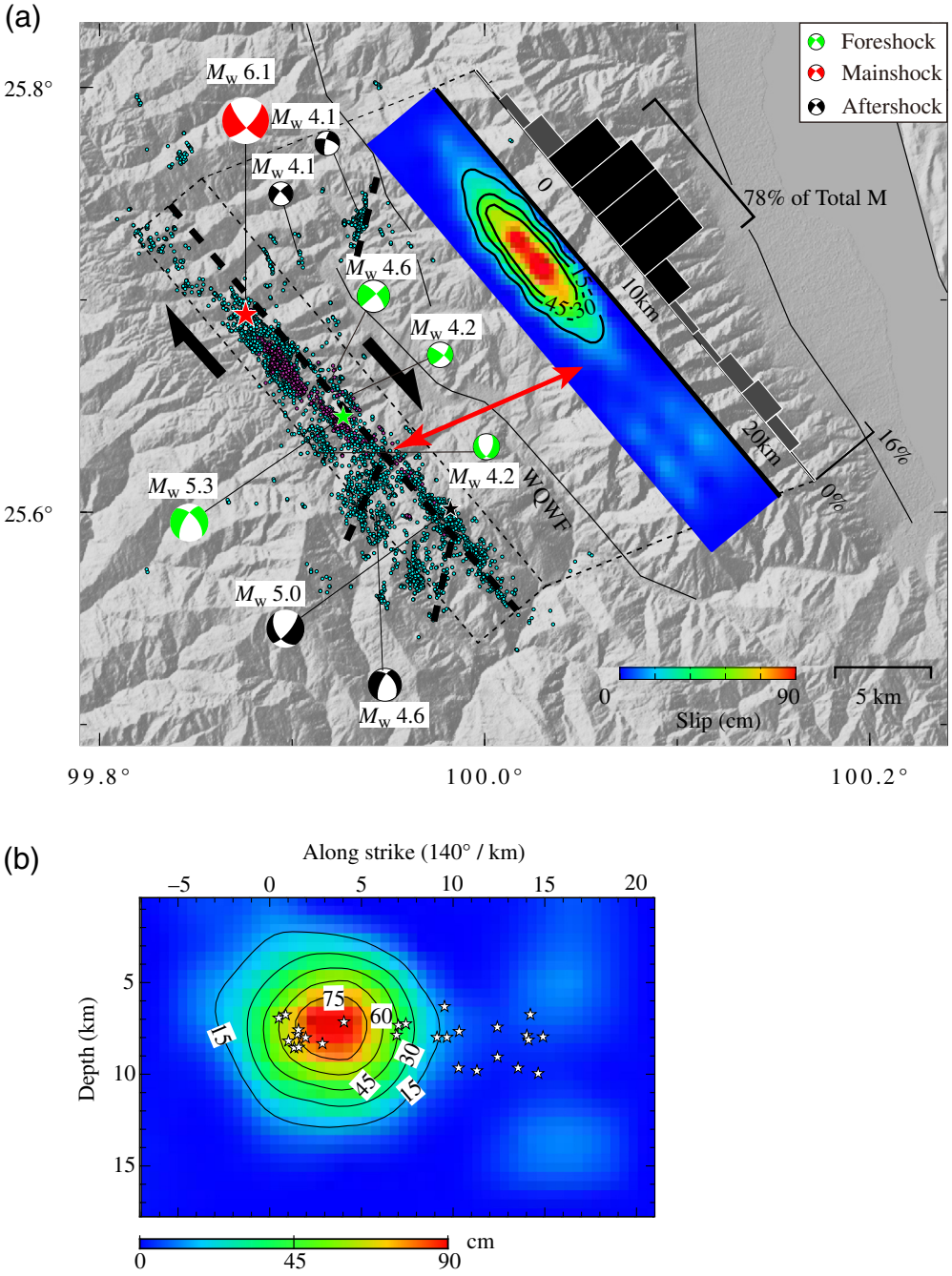

Figure 12. The comparison of our slip model with the relocated Yangbi earthquake sequence by Su *et al.* (2021). (a) The projection of slip distribution with the sequence. The foreshocks and aftershocks are plotted as purple dots and cyan dots, respectively. The green, red, and black circles denote the focal mechanisms of the foreshocks, the mainshock, and the aftershocks, respectively. The dashed rectangle represents the projection of the fault plane on the surface. Note that we move it about 3 km for the different mainshock's epicenter that is applied in this study. The color shows the slip value. The red star represents the epicenter of the mainshock. The contours with the interval of 15 cm up to 45 cm mark the dominant slip patch. The histogram represents the moment rate along the strike direction. The focal mechanisms of the mainshock, the largest foreshock (FS), and the largest aftershock (AS) are plotted. The black arrows show the slip direction of the mainshock. WQWF is the Weixi–Qiaohou–Weishan fault. The bold dashed lines are the suggested conjugate faults of mainshock and aftershocks. (b) The slip distribution of the Yangbi earthquake with the projection of aftershocks along-strike 140°. White stars represent aftershocks with a magnitude larger than M 3 within 24 hr after the mainshock (catalog from Su *et al.*, 2021). The color version of this figure is available only in the electronic edition.

from Zhang *et al.* (2021), and the catalog was obtained from Su *et al.* (2021). All figures were plotted by the Generic Mapping Tools (GMT), which was downloaded from the site https://github.com/GenericMappingTools/gmt/issues (last accessed July 2020). The general cut-and-paste (gCAP) code was downloaded from the site http://www.eas.slu.edu/People/LZhu/downloads/gcap1.0.tar (last accessed May 2018). The predicted *P* phase arrival time was calculated by tauP code, which was downloaded from http://www.seis.sc.edu/downloads/TauP/TauP-2.5.0.tgz (last accessed May 2021). The CRUST 2.0 crustal model was downloaded from the site https://igppweb.ucsd.edu/~gabi/crust2.html (last accessed May 2021). The information about an earthquake of magnitude 6.4 occurring in Yangbi County, Dali Prefecture, Yunnan is available at http://www.cea-igp.ac.cn/kydt/278248.html (last accessed November 2021). InSAR deformation research results of the M_s 6.4 Yangbi, Yunnan, earthquake are available at https://www.eq-igl.ac.cn/kydt/info/2021/33859.html (last accessed November 2021).

Declaration of Competing Interests

The authors acknowledge that there are no conflicts of interest recorded.

Acknowledgments

The authors acknowledge that the Data Management Centre (DMC) of China National Seismic Network at the Institute of Geophysics provided the data set. The authors thank Shiqing Xu and LingLing Ye for the constructive discussion. In addition, the authors thank Jinbo Su and Jinzhong Jiang for providing the relocation data of the Yangbi earthquake sequence. This work was financially supported by the Second Tibetan Plateau Scientific Expedition and Research Program

(STEP, Grant Number 2019QZKK0701), National Science Foundation of China (Grant Number 42074066, 41574058, 42130807), the Key Research Program of the Institute of Geology and Geophysics, Chinese Academy of Sciences, Grant Number IGGCAS-201904, and the Science and Technology Project of Yunnan Earthquake Agency (Grant Number 2021YBZX15, 2020ZX01).

References

Adams, M., J. Hao, and C. Ji (2019). Energy-based average stress drop and its uncertainty during the 2015 Mw 7.8 Nepal earthquake constrained by geodetic data and its implications to earthquake dynamics, *Geophys. J. Int.* **217,** no. 2, 784–797, doi: 10.1093/gji/ggz047.

Anderson, E. M. (1951). *The Dynamics of Faulting*, Second Ed., Oliver and Boyd, Edinburgh, Scotland, 206 pp.

Bassin, C., G. Laske, and G. Masters (2000). The current limits of resolution for surface wave tomography in North America, *Eos Trans. AGU* **81,** no. 48, F897.

Crotwell, H. P., T. J. Owens, and J. Ritsema (1999). The Taup Toolkit: Flexible seismic travel-time and ray-path utilities, *Seismol. Res. Lett.* **70,** no. 2, 154–160, doi: 10.1785/gssrl.70.2.154.

Fialko, Y., and Z. Jin (2021). Simple shear origin of the cross-faults ruptured in the 2019 Ridgecrest earthquake sequence, *Nat. Geosci.* **14,** 513–518, doi: 10.1038/s41561-021-00758-5.

Hao, J. L., and Z. X. Yao (2012). The coseismic displacement, strain and stress in the layered elastic model, *Chin. J. Geophys.* **55,** no. 5, 1682–1694, doi: 10.6038/j.issn.0001-5733.2012.05.025 (in Chinese).

Hao, J. L., C. Ji, W. Wang, and Z. Yao (2013). Rupture history of the 2013 M_w 6.6 Lushan earthquake constrained with local strong motion and teleseismic body and surface waves, *Geophys. Res. Lett.* **40,** no. 20, 5371–5376, doi: 10.1002/2013GL056876.

Hao, J. L., C. Ji, and Z. Yao (2017). Slip history of the 2016 Mw 7.0 Kumamoto earthquake: Intraplate rupture in complex tectonic environment, *Geophys. Res. Lett.* **44,** 743–750, doi: 10.1002/2016GL071543.

Huang, X. J., Z. H. Wu, J. C. Li, C. R. Nima, Y. H. Liu, X. L. Huang, and D. Zhang (2014). Tectonic geomorphology and Quaternary tectonic activity in the northwest Yunnan rift zone, *Geol. Bull. China* 33**,** no. 4, 578–593 (in Chinese).

Huangfu, G., J. Z. Qin, Z. H. Li, and C. D. Wu (2007). Subarea characteristics of earthquake type in Yunnan, *Acta Seismol. Sinica* 29**,** no. 2, 142–150 (in Chinese).

Ji, C., R. J. Archuleta, and C. Twardzik (2015). Rupture history of 2014 MW 6.0 South Napa earthquake inferred from near-fault strong motion data and its impact to the practice of ground strong motion prediction, *Geophys. Res. Lett.* **42,** no. 7, 2149–2156, doi: 10.1002/2015GL063335.

Ji, C., D. J. Wald, and D. V. Helmberger (2002a). Source description of the 1999 Hector Mine, California, earthquake, part I: Wavelet domain inversion theory and resolution analysis, *Bull. Seismol. Soc. Am.* **92,** no. 4, 1192–1207.

Ji, C., D. J. Wald, and D. V. Helmberger (2002b). Source description of the 1999 Hector Mine, California, earthquake, part II: Complexity of slip history, *Bull. Seismol. Soc. Am.* **92,** no. 4, 1208–1226.

Kanamori, H. (1977). The energy release in great earthquakes, *J. Geophys. Res.* **82,** no. 20, 2981–2987.

Li, C. Y., J. Y. Zhang, W. Wang, K. Sun, and X. J. Shan (2021). The seismogenic fault of the 2021 Yunnan Yangbi M_S 6.4 earthquake, *Seismol. Geol.* **43,** no. 3, 706–721, doi: 10.3969/j.issn.0253-4967.2021.03.015 (in Chinese).

Li, X., Y. K. Ran, L. C. Chen, H. Wang, J. Yu, Y. Q. Zhang, and Y. Q. Xie (2016). The Holocene seismic evidence on southern segment of the Red River fault zone, *Seismol. Geol.* 38**,** no. 3, 596–604 (in Chinese).

Lin, J., and R. S. Stein (2004). Stress triggering in thrust and subduction earthquakes and stress interaction between the southern San Andreas and nearby thrust and strike-slip faults, *J. Geophys. Res.* **09,** no. B2, doi: 10.1029/2003JB002607.

Liu, J. Q., W. J. Wang, G. M. Wang, Z. L. Wang, Y. Zhang, H. L. Cai, and Z. W. Li (2021). Seismic moment tensor and seismogenic structure of the Yangbi Ms 6.4 earthquake sequence on May 21, 2021 in Yunnan, *Chin. J. Geophys.* **64,** no. 12, 4475–4487, doi: 10.6038/cjg2021P0559 (in Chinese).

Long, F., P. Y. Qi, G. X. Yi, W. W. Wu, G. M. Wang, X. Y. Zhao, and G. L. Peng (2021). Relocation of the M_S 6.4 Yangbi earthquake sequence on May 21, 2021 in Yunnan Province and its seismogenic structure analysis, *Chin. J. Geophys.* **64,** no. 8, 2631–2646, doi: 10.6038/cjg2021O0526 (in Chinese).

Okada, Y. (1992). Internal deformation due to shear and tensile faults in a half-space, *Bull. Seismol. Soc. Am.* **82,** no. 2, 1018–1040.

Okubo, K., B. Harsha, R. Esteban, M. Samson, S. Alexandre, L. Zhou, K. Earl, and K. Yann (2019). Dynamics, radiation, and overall energy budget of earthquake rupture with coseismic off-fault damage, *J. Geophys. Res.* **124,** 11,771–11,801.

Parsons, T., R. S. Stein, R. W. Simpson, and P. A. Reasenberg (1999). Stress sensitivity of fault seismicity: A comparison between limited-offset oblique and major strike-slip faults, *J. Geophys. Res.* **104,** no. B9, 20,183–20,202.

Ross, Z. E., B. Idini, Z. Jia, O. L. Stephenson, M. Zhong, X. Wang, Z. Zhan, M. Simons, E. J. Fielding, S. H. Yun, *et al.* (2019). Hierarchical interlocked orthogonal faulting in the 2019 Ridgecrest earthquake sequence, *Science* **366,** no. 6463, 346–351, doi: 10.1126/science.aaz0109.

Shao, G., C. Ji, and E. Hauksson (2012). Rupture process and energy budget of the 29 July 2008 Mw 5.4 Chino Hills, California, earthquake, *J. Geophys. Res.* **117,** no. B7, doi: 10.1029/2011JB008856.

Su, J. B., M. Liu, Y. P. Zhang, W. T. Wang, H. Y. Li, J. Yang, X. B. Li, and M. Zhang (2021). High resolution earthquake catalog building for the 21 May 2021 Yangbi, Yunnan, M_S 6.4 earthquake sequence using deep-learning phase picker, *Chin. J. Geophys.* **64,** no. 8, 2647–2656, doi: 10.6038/cjg2021O0530 (in Chinese).

Thatcher, W., and D. P. Hill (1991). Fault orientations in extensional and conjugate strike-slip environments and their implications, *Geology* **19,** no. 11, 1116–1120.

Wang, S. J., Y. H. Liu, X. J. Shan, C. Y. Qu, G. H. Zhang, Z. D. Xie, D. Z. Zhao, X. R. Fan, J. Hua, S. M. Liang, *et al.* (2021). Coseismic surface deformation and slip models of the 2021 M_S 6.4 Yangbi (Yunnan, China) earthquake, *Seismol. Geol.* **43,** no. 3, 692–705, doi: 10.3969/j.issn.0253-4967.2021.03.014 (in Chinese).

Wang, Y., S. Q. Hu, X. H. He, K. Guo, M. Y. Jie, S. G. Deng, and Y. W. Ma (2021). Relocation and focal mechanism solutions of the 21 May 2021 *Ms* 6.4 Yunnan Yangbi earthquake sequence, *Chin. J. Geophys.* **64,** no. 12, 4510–4525, doi: 10.6038/cjg2021P0401 (in Chinese).

Wang, Y., H. Ran, Q. L. Li, C. P. Zhao, L. S. Guo, and Y. W. Liu (2019). A study on characteristics of geothermal and tectonic activities in the Northwest Yunnan Rifting Zone, Western China, *Bull. Mineral. Petrol. Geochem.* 38**,** no. 5, 923–930 (in Chinese).

Wei, S. J., M. Chen, X. Wang, R. W. Graves, E. Lindsey, T. Wang, Ç. Karakaş, and D. Helmberger (2018). The 2015 Gorkha (Nepal) earthquake sequence: I. Source modeling and deterministic 3D ground shaking, *Tectonophysics* **722,** 447–461, doi: 10.1016/j.tecto.2017.11.024.

Xie, X., and Z. X. Yao (1989). A generalized reflection-transmission coefficient matrix method to calculate static displacement field of a dislocation source in a stratified half space, *Chin. J. Geophys.* 32**,** no. 2, 191–205 (in Chinese).

Xu, S. (2020). Recognizing fracture pattern signatures contributed by seismic loadings, *Interpretation* **8,** no. 4, SP95–SP108, doi: 10.1190/INT-2020-0033.1.

Xu, S., and Y. Ben-Zion (2013). Numerical and theoretical analyses of in-plane dynamic rupture on a frictional interface and off-fault yielding patterns at different scales, *Geophys. J. Int.* **193,** no. 1, 304–320, doi: 10.1093/gji/ggs105.

Xu, J., H. M. Zhang, and X. F. Chen (2015). Rupture phase diagrams for a planar fault in 3-D full-space and half-space, *Geophys. J. Int.*, **202,** no. 3, 2194–2206, doi: 10.1093/gji/ggv284.

Xu, T., M. H. Zhang, X. B. Tian, Y. Zheng, Z. M. Bai, C. L. Wu, Z. J. Zhang, and J. W. Teng (2014). Upper crustal velocity of Lijiang-Qingzhen profile and its relationship with the seismogenic environment of the M_S 6.5 Ludian earthquake, *Chin. J. Geophys.* **57,** no. 9, 3069–3079, doi: 10.6038/cjg20140932 (in Chinese).

Xu, T., Z. J. Zhang, B. F. Liu, Y. Chen, M. H. Zhang, X. B. Tian, Y. G. Xu, and J. W. Teng (2015). Crustal velocity structure in the Emeishan Large Igneous Province and evidence of the Permian mantle plume activity, *Sci. China Earth Sci.* **58,** no. 7, 1133–1147, doi: 10.1007/s11430-015-5094-6.

Yamanaka, Y., and M. Kikuchi (2004), Asperity map along the subduction zone in northeastern Japan inferred from regional seismic data, *J. Geophys. Res.* **109,** no. B7, doi: 10.1029/2003JB002683.

Yang, Z. G., J. Liu, X. M. Zhang, W. Z. Deng, G. B. Du, and X. Y. Wu (2021). A preliminary report of the Yangbi, Yunnan, MS6.4 earthquake of May 21, 2021, *Earth Planet. Phys.* **5,** no. 4, 1–3, doi: 10.26464/epp2021036.

Ye, L. L., T. Lay, Y. Bai, K. F. Cheung, and H. Kanamori (2017). The 2017 M_w 8.2 Chiapas, Mexico, earthquake: Energetic slab detachment, *Geophys. Res. Lett.* **44,** 11,824–11,832, doi: 10.1002/2017GL076085.

Yue, H., T. Lay, and K. D. Koper (2012). En échelon and orthogonal fault ruptures of the 11 April 2012 great intraplate earthquakes, *Nature* **490,** no. 7419, 245–249, doi: 10.1038/nature11492.

Zhang, K. L., W. J. Gan, S. M. Liang, G. R. Xiao, C. L. Dai, Y. B. Wang, C. J. Li, L. Zhang, and G. Q. Ma (2021). Coseismic displacement and slip distribution of the 2021 May 21, M_S 6.4, Yangbi Earthquake derived from GNSS observations, *Chin. J. Geophys.* **64,** no. 7, 2253–2266, doi: 10.6038/cjg2021O0524 (in Chinese).

Zhu, L. P., and Y. Ben-Zion (2013). Parametrization of general seismic potency and moment tensors for source inversion of seismic waveform data, *Geophys. J. Int.* **194,** no. 2, 839–843, doi: 10.1093/gji/ggt137.

Zhu, L. P., and L. A. Rivera (2002). A note on the dynamic and static displacements from a point source in multilayered media, *Geophys. J. Int.* **148,** no. 3, 619–627.

Manuscript received 30 August 2021
Published online 24 March 2022